

Green Chemistry

Accepted Manuscript



This is an *Accepted Manuscript*, which has been through the Royal Society of Chemistry peer review process and has been accepted for publication.

Accepted Manuscripts are published online shortly after acceptance, before technical editing, formatting and proof reading. Using this free service, authors can make their results available to the community, in citable form, before we publish the edited article. We will replace this *Accepted Manuscript* with the edited and formatted *Advance Article* as soon as it is available.

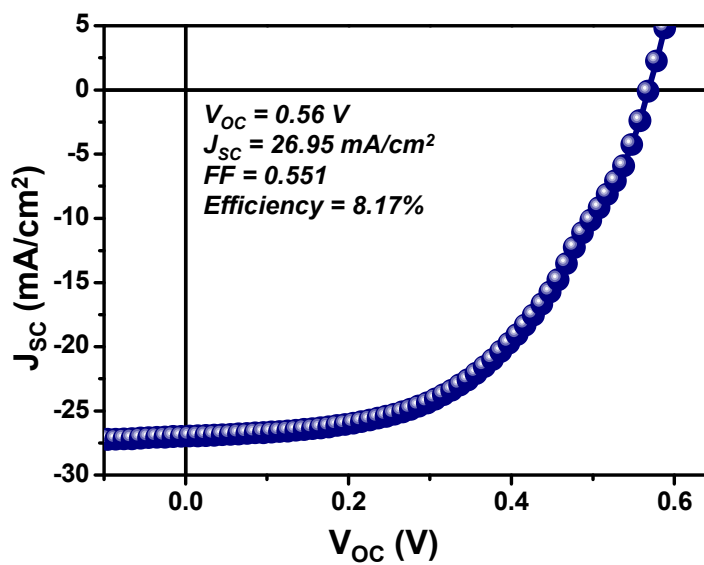
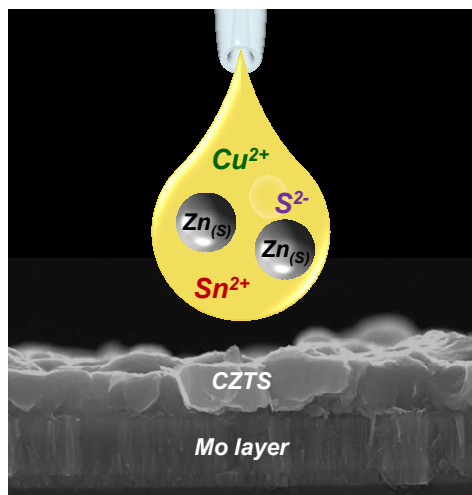
You can find more information about *Accepted Manuscripts* in the [Information for Authors](#).

Please note that technical editing may introduce minor changes to the text and/or graphics, which may alter content. The journal's standard [Terms & Conditions](#) and the [Ethical guidelines](#) still apply. In no event shall the Royal Society of Chemistry be held responsible for any errors or omissions in this *Accepted Manuscript* or any consequences arising from the use of any information it contains.



www.rsc.org/greenchem

Table of contents entry



A $\text{Cu}_2\text{ZnSnS}_4$ solar cell with an efficiency of 8.17% is fabricated using a non-toxic solvent-based hybrid-ink without the involvement of complex synthesis, toxic solvents or harmful post-selenization.

Influence of Precursor Type in Non-Toxic Hybrid Inks for High-Efficiency $\text{Cu}_2\text{ZnSnS}_4$ Thin-Film Solar Cells

Cite this: DOI: 10.1039/x0xx00000x

Received 00th January 2014,
Accepted 00th January 2014

DOI: 10.1039/x0xx00000x

www.rsc.org/

Kyujin Kim,^a Inhyuk Kim,^a Yunjung Oh,^a Daehee Lee,^a Kyoohye Woo,^b Sunho Jeong,^c and Jooho Moon^{a,*}

Copper zinc tin sulfide (CZTS) has attracted significant attention in the past few years as a next-generation absorber material, and it is a promising candidate for the mass production of thin-film solar cells with high efficiencies. Here, we demonstrate a non-toxic solvent-based hybrid-ink approach for the fabrication of a high-quality CZTS absorber layer with a thickness of 1.3 μm and micrometer-scale grains ($\sim 1 \mu\text{m}$), resulting in an efficiency of 8.17%. In particular, we investigate the effects of the solid-state Zn metal or ZnS precursor on both the phase transformation and the device performance, which clearly suggests that the low-melting-point Zn phase effectively facilitates the phase-pure, high-performance CZTS absorber layer without the formation of secondary phases that have been observed in most cases of CZTS solar cells derived from wet chemical processes. We believe that our environmentally friendly approach will pave the way toward achieving low-cost, scalable solar cells with high efficiencies.

1. Introduction

Kesterite $\text{Cu}_2\text{ZnSn}(\text{S},\text{Se})_4$ (CZTSSe) is considered one of the most attractive materials to serve as an alternative over conventional $\text{Cu}(\text{In},\text{Ga})(\text{S},\text{Se})_2$ -based absorber layers because CZTS is composed of earth-abundant and environmentally friendly constituents. It has an optimal direct band gap (1.0 – 1.5 eV) and a high absorption coefficient of 10^4 cm^{-1} .¹⁻⁹ To date, CZTS thin films have been prepared using two methods: vacuum-based and non-vacuum solution-based processes. Vacuum-based technologies such as co-evaporation¹⁰ and sputtering¹¹ allow precise control of both the composition of the overall film and the phase profile along the film thickness. However,

both methods are unfit, to some extent, for the cost-effective commercialization of large-area solar cells. Alternatively, non-vacuum solution-based approaches, including electrodeposition,¹² nanocrystal ink,¹³ and hydrazine-based ink,¹⁴⁻¹⁶ could enable a low-cost route to the fabrication of these optoelectronically active devices because of their large-area deposition capabilities.¹⁷⁻¹⁸ Among the proposed techniques, the hydrazine-based hybrid-ink approach has received significant recent interest, which demonstrates the potential of solution-processed, highly efficient CZTSSe solar cells.¹⁹⁻²² Hydrazine (N₂H₄) is a carbon- and oxygen-free ideal solvent medium in which metal chalcogenides could be dissolved. This approach would eliminate the possibility of incorporating impurities. In hydrazine-based hybrid methodologies, Cu and Sn elemental constituents are dissolved with no additives, and ZnS nanoparticles are suspended in a precursor solution, acting as stress-relief and crack-deflection centers. This unique combination in an ink preparation enables the fabrication of highly pure and precisely stoichiometry-controlled CZTSSe films, leading to a maximum efficiency of 12.6%.¹⁹ However, hydrazine is highly toxic and explosive in practical usage, which has stimulated the development of non-hydrazine, non-toxic, environmentally friendly, solution-based approaches.¹⁹⁻²²

A wide variety of alternative solvents have been explored to preclude the use of hydrazine. The Yang group developed a clear solution in which all precursors were dissolved in a mixture of ethanolamine and dimethylsulfoxide (DMSO). This procedure led to solution-deposited CZTSSe solar cells with efficiencies of 7.5%.²² However, this approach still required hydrazine to synthesize the relevant hydrazinium complexes that were soluble in the mixed solvent. Metal salt-based sol-gel methods, in which either 2-methoxyethanol, water, or DMSO were utilized as solvents, have resulted in CZTSSe devices with efficiencies of 5.1 – 7.5%.²³⁻²⁵ Apart from the all-soluble precursor-based methods, we have previously reported a non-toxic solvent-based slurry approach in which all commercially available precursor particles were suspended in ethanol, resulting in 7.1% efficient

CZTSSe cells.²⁶ However, it should be noted that most of the prior research has exploited post-selenization processes in an extremely toxic Se atmosphere for the adjustment of the absorber layer band gap. Considering this, it is beneficial to develop highly efficient pure sulfide $\text{Cu}_2\text{ZnSnS}_4$ (CZTS) solar cells without incorporating a harmful selenization process. To date, electrodeposited and selenization-free CZTS devices have been demonstrated with efficiencies of 7.99%.²⁷ For solution-derived CZTS solar cells, the efficiencies have been limited to 5.14–5.29%.^{28,29}

We present a non-toxic solvent-based hybrid-ink approach that retains the advantage associated with soluble/insoluble phase-mixed hybrid methods in producing highly efficient CZTS solar cells. Our hybrid inks are prepared with 2-methoxyethanol, an environmentally benign solvent, because it can evaporate quickly and thereby minimize the presence of residual carbon- or oxygen-containing impurities in the film. Cu and Sn precursors are completely dissolved in 2-methoxyethanol by complexation with thiourea,^{23,30} and an insoluble Zn precursor is employed in the precursor solution containing Cu and Sn components to form hybrid-type inks. We disperse either Zn metal or ZnS (here onwards denoted as ZM and ZS, respectively) particles as a Zn precursor, with an emphasis on investigating the influence of solid precursors in hybrid inks on both the phase transition and the device performance. Other types of solid-state Zn sources, such as ZnO and $\text{Zn}(\text{OH})_2$, are not employed to prevent the precursors from being present as an oxide phase or from oxidizing into an oxide phase during annealing; if this were the case, an additional reducing step would be required. After an in-depth study on the critical role of ZM as a low melting point phase, the resulting CZTS photovoltaic devices can be observed to demonstrate a power conversion efficiency (PCE) of 8.17%. This result indicates that our approach is potentially viable for fabricating CZTS solar cells without the involvement of complex synthesis, a highly toxic solvent, and

harmful selenization. In particular, our non-toxic solvent based hybrid approach is cost effective with respect to with hydrazine based slurry approach. The amount of waste stream is supposed to be similar, because the absorber layers are fabricated by a spin coating method in both approaches. However, the hydrazine must be handled using appropriate protective equipment to prevent the physical contact with either a vapor or a liquid, because hydrazine is extremely toxic and dangerously unstable. Indeed, in terms of bio-degradability, which represents the chemical dissolution of materials by bacteria or other biological means without harmful residue, the bio-degradability of hydrazine solvent is about 28%, which is quite lower than that of 2-methoxyethanol (~ 97%) (Figure S1, †Electronic Supplementary Information (ESI)). These values suggest that our hybrid ink would significantly reduce the amount of hazardous waste treatment by ~ 96% as compared with hydrazine based slurry.

2. Results and discussion

Fig. 1a shows X-ray diffraction (XRD) patterns of ZM hybrid ink-derived films annealed under a H₂S atmosphere at different temperatures. All samples were pre-annealed at 250 °C in a H₂/Ar atmosphere. For the sulfurization process, the Ar gas was supplied during a ramping period, and H₂S gas was supplied upon approaching a desired temperature. At sulfurization temperatures ranging from 250 to 350 °C, the diffraction peaks at the 2θ values of 26.6° and 30.2°, corresponding to Cu₂SnS₃ with the wurtzite structure (JCPDS 27-0198, denoted as WZ)³¹, were mainly observed, along with a zinc blende Cu₂SnS₃ phase (JCPDS 33-0501, denoted as ZB)³¹ at 28.45°, 47.3° and 56.2°. At temperatures above 400 °C, it was clearly observed that the peak at 26.6° disappeared and that the diffraction peaks at 28.45°, 32.98°, 47.3° and 56.2° evolved, which implies the formation of the CZTS phase (JCPDS 26-0575) at the expense of Cu₂SnS₃, even at relatively low temperatures. The formation enthalpy of the ZnS phase is lower than those of other binary sulfide compounds (e.g., CuS, Cu₂S, SnS, and SnS₂), which suggests

that ZnS most likely forms during a sulfurization process³⁸ but that the ZnS phase cannot be precisely detected in XRD spectra as a result of the low crystallinity of the corresponding phases and the ambiguity in individually identifying the CZTS, Cu₂SnS₃, and ZnS phases in the XRD spectra. However, it can be presumed that the formation of Zn-related phases, which involves an elemental loss in the form of volatile phases, did not evolve because the composition did not vary after sulfurization at elevated temperatures. The Cu:Zn:Sn compositional ratios were measured to be 1.78:1.1:1 and 1.77:1.1:1 for films pre-annealed at 250 °C and sulfurized at 550 °C, respectively. For the case of ZS hybrid ink-derived films, the thermal behavior in crystalline phase transformations differed from that of the ZM hybrid ink-based films (Fig. 1b). Both the wurtzite and zinc blende structured Cu₂SnS₃ phases co-existed when the film was sulfurized at temperatures as high as 400 °C, and the kesterite CZTS phase was observed only above 450 °C, unlike the ZM hybrid ink-derived film, for which the kesterite phase began to appear at 400 °C. However, it should be noted that the peaks at approximately $2\theta = 28.45^\circ$, 47.3° and 56.2° overlap with the CZTS, Cu₂SnS₃, and ZnS phase characteristic peaks in the XRD spectrum, such that the phase purity of CZTS cannot be confirmed solely using XRD analysis. Therefore, Raman spectroscopy was utilized to assist with phase identification.

Fig. 2 shows Raman spectra measured using a 514 nm excitation wavelength. After sulfurization at 250 °C, the ZM hybrid ink-derived film exhibited peaks at 290, 312, 331, and 352 cm⁻¹, all of which are attributed to Cu₂SnS₃ (Fig. 2a).³³ The Cu₂SnS₃ peaks in the zinc blende and wurtzite structures cannot be distinguished because of peak overlapping at 300 – 350 cm⁻¹.³⁴ At a sulfurization temperature of 350 °C, most of the peaks related to Cu₂SnS₃ (*i.e.*, at 290 and 331 cm⁻¹) disappeared, whereas the peaks at 287, 338, and 359 cm⁻¹ ascribed to CZTS were detected. This result is indicative of the formation of CZTS together with Cu₂SnS₃ as a minor phase. Above 400 °C, all detected peaks were assigned to kesterite CZTS, which correlated well with the XRD analysis.³³⁻³⁵ In

the case of ZS hybrid ink-derived film sulfurized at 250 – 350 °C, the ZnS phase was observed at 353 cm⁻¹ together with the Cu₂SnS₃ phase. This result was indicated by peaks at 297 and 331 cm⁻¹ (Fig. 2b). At 400 °C, Cu₃SnS₄ (or Cu₅Sn₂S₇) was also detected by the peak at 312 cm⁻¹,³² and phase-pure CZTS appeared at a sulfurization temperature above 450 °C. The ZnS is a well-known secondary phase present in solution-processed CZTS or in CZTSSe absorber layers,^{10, 32-34} but it is difficult to precisely monitor the ZnS phase using Raman spectra with a 514 nm excitation wavelength. For further phase elucidation, we performed Raman analysis with a 325 nm excitation wavelength similar to the ZnS band gap (~3.7 eV). In this case, strong resonant Raman scattering made it possible to detect even traces of ZnS.³³⁻³⁵ The ZM hybrid ink-derived film exhibited only the CZTS phase at 338 cm⁻¹ without showing any ZnS phase when exposed to sulfurization temperatures ranging from 350 to 550 °C (Fig. 2c). By contrast, the ZnS phase was identified by peaks at 350 and 700 cm⁻¹ in ZS hybrid ink-derived films regardless of the annealing temperatures (Fig. 2d). The ZnS remained as an impurity even when the film was annealed to 550 °C.

The different reaction pathways in crystalline structural transformations toward a phase-pure CZTS layer were also confirmed by a thermo-gravimetric (TG) analysis in an inert atmosphere coupled with differential scanning calorimetry (DSC). As shown in Fig. 3a, the ZM hybrid ink involved a weight loss of ~2% with an exothermic peak at ~200 °C, attributable to the decomposition of dissolved precursors. Broad endothermic peak at ~250 °C is likely a result of the crystallization of Cu₂SnS₃, as indicated by the XRD and Raman analyses. The sharp endothermic peak at ~320 °C would result from the melting of metallic Zn. It is possible that the metallic Zn particles with a diameter of ~70 nm melt at temperatures lower than the melting point of the bulk phase (420 °C).³⁶ This characteristic melting behavior of metallic Zn nanoparticles reveals the evolution of a reactive liquid phase surrounding the Cu-Sn-S precursor phases during a ramping stage in Ar atmosphere. Zn melting may induce a

capillary force that pulls the particles together, leading the microstructural rearrangement toward more packed particulate films. When the H₂S gas was supplied at high temperatures above 350 °C, the vigorous liquid phase diffusion and chemical reaction with vapor S molecules enabled a dense and phase-pure kesterite CZTS film to form, without leaving any secondary phases—including the ZnS phase. Reduced weight loss was observed until 400 °C using the ZS hybrid ink, although the overall loss was similar to that of ZM hybrid ink. Two small endothermic inflection points were observed at 443 °C and 475 °C, with no sharp endothermic peak at ~320 °C. Furthermore, the heat flow above 350 °C decayed more gradually than that of ZM hybrid ink. This result may indicate a sluggish phase transformation from the ZS hybrid layer to the CZTS film. The ZnS phase presented in ZS hybrid films has a relatively high melting point of 1185 °C. It is therefore possible that the ZnS particles remain intact in a solid state during the sulfurization process. This solid-state reaction, even when involved with a gas phase reaction with H₂S molecules, would retard the CZTS phase transformation, instead converting the preformed Cu₂SnS₃ phase into a Cu₃SnS₄ or a Cu₅Sn₂S₇ phase. At sulfurization temperatures as high as 450 °C, ZnS began to take part in a reaction with the Cu₂SnS₃, Cu₃SnS₄ or Cu₅Sn₂S₇ phases, from which the kesterite CZTS phase formed through a multi-step phase formation. Small endothermic inflection points in the TG-DSC indicated this phenomenon, which resulted in unreacted ZnS secondary phases.

Fig. 4 shows the microstructural evolution of non-toxic hybrid ink-derived absorbers after a sulfurization at 550 °C. Both the ZM and ZS hybrid ink-derived films exhibited dense microstructures with large grains (> 1 μm). To investigate the compositional uniformity, the lateral compositional distributions in the top surfaces of both films were determined using energy-dispersive X-ray spectroscopy (EDX). It was revealed that whereas the composition uniformity was obtainable in a ZM hybrid ink-derived film (Fig. 4a), the bright domain in an elemental map of Zn, indicative of a lump of Zn, was distinctively detected in a ZS hybrid ink-derived film (Fig. 4b). This result is in

accordance with the analytical result obtained by Raman spectroscopy. Cross-sectional images of the ZM hybrid- and ZS hybrid ink-derived films are shown in Fig. 4c and d, respectively. Both films had uniformly dense structures without large pores and cracks. However, as observed in the interfacial morphology (shown as inset images), the needle-like segregated phase was observed only in the ZS hybrid ink-derived CZTS films. The thickness of the MoS₂ in the ZS hybrid ink-derived CZTS films is thicker than that in the ZM hybrid-ink derived CZTS films.

The CZTS absorber layers, prepared after a sulfurization at 550 °C, were employed during the fabrication of complete thin-film solar cells. Fig. 5a shows the cross-sectional SEM image for a complete CZTS solar cell with a ZM hybrid ink-derived absorber layer. The current density-voltage (J - V) characteristic of the highest performing CZTS solar cell under AM 1.5 illumination is shown in Fig. 5b, and the cell performance parameters are summarized in Table 1. The ZM hybrid ink-derived device, which had an effective area of 0.23 cm², exhibited an efficiency of 8.17% [open-circuit voltage (V_{OC}) = 0.56 V, short-circuit current density (J_{SC}) = 26.95 mA cm⁻², fill factor (FF) = 55.17%]. The narrow performance deviation was also confirmed by a reproducibly high efficiency that exceeded 8% (Table S1, †ESI). The device employing the ZS hybrid ink-derived CZTS layer had an efficiency of 5.38%, which was characterized by a lower V_{OC} and a higher R_s compared with the ZM hybrid ink-derived counterpart. It is speculated that these values are attributed predominantly to the presence of ZnS as a secondary phase in an absorber layer.^{35, 40} The ZnS phase has a higher band gap than CZTS, such that it could act as a resistance layer to impede charge carrier drift.^{10, 35} The external quantum efficiency (EQE) as a function of a photon wavelength is shown in Fig. 5c. EQE analysis indicated that the ZS hybrid-ink-derived cell suffered from quantum efficiency loss compared with ZM-based devices. This result is represented by a steep downslope after the maximum quantum efficiency. The EQE spectra at short wavelengths (below ~540 nm) are slightly poorer than

those reported by others because the buffer layer thickness used was ~60 nm. For ZM hybrid ink-derived cells, the maximum quantum efficiency of 82% was obtained at a photon wavelength of 540 nm, and the band gap was determined to be 1.46 eV from the EQE spectra by fitting a plot of $[E \ln(1-EQE)]^2$ vs. E near the band edge. The ZS hybrid ink-based device had a maximum quantum efficiency of 74% at 540 nm, with a band gap of 1.52 eV. The ratio of EQE at -1 and 0 V, or $[EQE(-1.0 \text{ V})/EQE(0.0 \text{ V})]$, is indicative of the degree of carrier collection efficiency. In general, the minority carrier suffers from ineffective charge collection without external bias since its diffusion length is relatively short. By applying -1 V reverse bias, the depletion region can extend to assist the minority carrier to be effectively collected, which raise the EQE response. Consequently, the $EQE(-1 \text{ V})/EQE(0 \text{ V})$ ratio above 1 suggests that the cell has a poor minority-carrier collection, particularly deep in the absorber layer. By contrast, the equivalent value, i.e., a ratio of 1, implies the good charge collection.³⁹ Better absorber quality was clearly observed in the EQE bias-ratio plot of ZM hybrid ink-based cell as the ratio remained close to the equivalent value without deviation (Fig. 5c). However, the bias ratio of ZS-based solar cells significantly increased above unity at long wavelengths, implying incomplete carrier collection. This ineffective collection behavior has been previously observed for CZTS cells and CIGSSe devices with large band gap energy. This poor carrier collection efficiency is ascribed to a short carrier lifetime, which results from a high defect density in an absorber layer and higher recombination loss at a back contact or at a front interface.³⁹⁻⁴³

In order to ascertain the cause of low carrier lifetime which limits V_{OC} , the temperature-dependent transport characteristics were also investigated. It was observed that the efficiencies of the ZM hybrid- and ZS hybrid ink-derived CZTS gradually decreased from 300 to 113 K, concurrent with a linear increase in V_{OC} (Fig. 6a and b). The relationship between V_{OC} and temperature is generally given as follows:

$$V_{OC} = \frac{E_A}{q} - \frac{AkT}{q} \ln \frac{J_{OO}}{J_L}$$

where E_A , A , J_{OO} , and J_L are the activation energy of the dominant recombination mechanism, the diode ideality factor, the reverse saturation current pre-factor, and the photocurrent, respectively.³⁹ In well-behaved solar cells, the activation energy should be equal to the band gap of the absorber layer indicating the main recombination mechanism arises in the space charge region (SCR) of the absorber layer.³⁹⁻⁴³ If value of activation energy is low compared to that of band gap, recombination for the CZTS devices could occur at CdS/CZTS interface, defect in the interface or a cliff-type band alignment, where the conduction band edge of the absorber layer is higher than that of the buffer layer. To provide better explanation for the recombination mechanism difference associated with ZM hybrid- and ZS hybrid-ink derived CZTS devices, energy level diagrams are illustrated in Figure S2 (†ESI). The activation energy, $E_A = qV_{OC}$ (~1.41 eV), extracted from the extrapolation of V_{OC} to $T = 0$ K, was similar to the band gap value ($E_g = 1.46$ eV) obtained from the EQE data for ZM hybrid ink-derived cells. However, lower activation energy (~1.32 eV) compared with E_g (1.52 eV) was observed for the ZS hybrid ink-derived device. This fact suggests that the main recombination mechanism is dominated by an interface recombination for ZS hybrid ink-derived CZTS cells, which acts as a limiting factor for V_{OC} . The general interface recombination for the CZTS solar cell occurs at the interface of CdS/CZTS or at the MoS₂ layer of CZTS/Mo interface.^{10,39} Therefore, this lower activation energy is indicative of an additional interface recombination mechanism, which might relate to a thick MoS₂ layer and a ZnS impurity phase in the ZS hybrid ink-derived CZTS cell, as confirmed by XRD, Raman, and compositional analyses. ZnS phases were remained as residue after sulfurization which could act as blocking layer and disturb carrier collection which formed at near bottom of absorber layer. Below 213 K, as shown in Fig. 6b, c and d, the fill factor and short-circuit current dropped dramatically, while the series resistance (R_S) increased greatly. This behavior resulted in an efficiency collapse as the temperature approached zero. R_S of the ZS hybrid ink-derived

CZTS cell increased by as much as ~28 times from 300 to 113 K, compared with only ~12 times for the ZM hybrid ink-derived CZTS cell. One plausible reason for this diverging series resistance at low temperatures is the formation of a blocking back contact in the form of a thick MoS₂ layer (Fig. 4d) at the interface between the Mo and CZTS. This development might suppress the majority carrier (hole) transport. The presence of the high band gap ZnS in the ZS hybrid ink-derived cell is also implicated because the ZnS phase suppresses carrier transport behavior.³⁹⁻⁴³

3. Conclusions

We developed a non-toxic solvent-based hybrid-ink approach that precluded the use of toxic solvents and a harmful selenization process for the production of 8.17% efficient CZTS solar cells. This readily achievable hybrid ink can be produced without the involvement of complex particle synthesis. It enables a convenient methodology to be applied in the process of fabricating a high-quality CZTS absorber layer. We also investigated the influence of a solid-state Zn precursor incorporated with soluble Cu-Sn-S precursors on both the phase formation and device performance. It was revealed that well-dispersed metallic Zn nanoparticles undergo melting at ~320 °C, facilitating the formation of a dense, phase-pure kesterite CZTS film above 400 °C. By contrast, the ZnS particles that remained in the solid state, even at elevated temperatures below 550 °C, retarded the CZTS phase transformation, resulting in secondary phase-involved CZTS absorber layers. Distinct phase and microstructural evolutions that depended on the type of Zn solid component enabled their influence on device performance to be understood. The presence of the ZnS secondary phase plays a critical role in reducing the carrier lifetime, as well as lowering the V_{OC} , both of which impair the device performance as compared with that of a ZM hybrid ink-derived cell.

4. Experimental

In a 50 mL glass vial, 1.428 M of copper (II) chloride anhydrous (CuCl_2 , Sigma-Aldrich, 99.995%), 0.8 M of tin (II) chloride dihydrate ($\text{SnCl}_2 \cdot 2\text{H}_2\text{O}$, Sigma-Aldrich, 99.995%), and 4.8 M of thiourea ($\text{SC}(\text{NH}_2)_2$, Sigma-Aldrich, 99.0%) were dissolved in 2-methoxyethanol ($\text{C}_3\text{H}_8\text{O}_2$, Sigma-Aldrich, 99.8%). The resultant opaque solution was stirred for 30 min at room temperature to prepare transparent yellow Cu-Sn-S precursor solution. This solution was stable for at least several months. Either 0.88 M of zinc particles (the average particle size ~ 70 nm, Sigma-Aldrich, 99%) or zinc sulfide particles (the average particle size ~ 80 nm, Sigma-Aldrich, 99%) was mixed into the Cu-Sn-S solution with 3 wt% of polyvinylpyrrolidone (PVP, $M_w \sim 10,000$), followed by a planetary milling for 3 h to obtain two different CZTS hybrid inks. We accomplished the improvement in the dispersion property of either Zn or ZnS particles in the ink as the agglomerate particles were separated by the physical impact when the balls rotated along the direction of cylindrical vessel. Both formulated inks retained a composition that was poor in Cu and rich in Zn (*i.e.*, $\text{Cu}/(\text{Zn} + \text{Sn}) = 0.85$ and $\text{Zn}/\text{Sn} = 1.1$). The hybrid inks were coated on Mo-deposited soda lime glass substrates using a spin-coating method. Three consecutive coatings at 7000 rpm for 25 s were employed to achieve a film thickness of approximately 1.3 μm . The precursor film was pre-annealed at 250 $^\circ\text{C}$ in a reductive atmosphere consisting of H_2 (5%) + Ar. To fabricate the highly efficient CZTS solar cells, the absorber layers were annealed at 550 $^\circ\text{C}$ under H_2S (5%) + Ar with a controlled growth strategy to achieve highly dense and pinhole-free layers and large grains. To investigate the CZTS phase formation pathway that depended upon the precursor type in the hybrid inks, the films were sulfurized at temperatures that ranged from 250 $^\circ\text{C}$ to 550 $^\circ\text{C}$. The annealing process consisted of treatment in an inert atmosphere during the ramp up, followed by sulfurization for 30 min under H_2S (5%) + Ar at the final temperatures.

The annealed CZTS films were processed into photovoltaic devices following standard procedures with the structure of ITO/*i*-ZnO/CZTS/Mo/SLG. The transparent conductive oxide (TCO) layer was deposited using a sputtering. The CdS layer improving the lattice matching between the absorber and n-doped layer was deposited by chemical bath deposition process with a thickness of 60 nm. The 50 nm-thick *i*-ZnO and 200 nm-thick ITO transparent conductor layers were sputtered on top of CdS layer. The thermal behavior of the precursor inks in the argon atmosphere was examined using thermo-gravimetry coupled with differential scanning calorimetry in an argon atmosphere (SDT Q600, TA Instruments). The microstructure of the sulfurized films was observed using a field effect scanning electron microscope (FESEM, JSM-6701F, ZEOL). The phase and crystal structures of the CZTS films were confirmed using X-ray diffraction (XRD, D/Max-2500H, Rigaku) and Raman spectroscopy (Lab Ram ARAMIS, Horriba Jovin Yvon) that used excitation wavelengths of 514 nm and 325 nm. The chemical compositions of the final CZTS films were measured using a FESEM equipped with energy-dispersive X-ray spectroscopy (EDX, JSM-6701F, JEOL). The current density-voltage (J - V) characteristics of the CZTS-based cells were analyzed using a solar simulator (Oriel Sol3A Class AAA, Newport Corporation). An incident photon conversion efficiency (IPCE) measurement unit (QEX 10, PV Measurements, Inc.) measured the external quantum efficiency (EQE) and the absorption behavior. For the low-temperature study, the cells were placed in a Linkam LTS420E temperature stage controlled by the T95-HS LinkPad (Linkam Scientific Instruments Ltd.) to measure the J - V curve at temperatures ranging from 113 – 300 K.

Acknowledgements

This research received financial support from a National Research Foundation of Korea (NRF) grant funded by the Korea government (MSIP) (no. 2012R1A3A2026417). It was also partially supported by the third stage of the Brain Korea 21 Plus Project.

Notes and references

^a Department of Materials Science and Engineering, Yonsei University, 50 Yonsei-ro Seodaemun-gu, Seoul 120-749, Republic of Korea. Fax: +82-2-312-5375; Tel.: +82-2-2123-2855; E-mail: jmoon@yonsei.ac.kr

^b Advanced Manufacturing Systems Research Division, Korea Institute of Machinery and Materials (KIMM), 156 Gajeongbuk-ro, Yuseong-gu, Daejeon 305-343, Republic of Korea

^c Device Materials Research Center, Korea Research Institute of Chemical Technology (KRICT), 19 Sinseongno, Yuseong-gu, Daejeon 305-600, Republic of Korea

†Electronic Supplementary Information (ESI) available: Bio-degradability value of solvents, the variation of device performance and energy level diagram and for ZM and ZS hybrid ink-derived CZTS. See DOI: 10.1039/b000000x/

- 1 T. K. Todorov, O. Gunawan, T. Gokmen and D. B. Mitzi, *Prog. Photovoltaics: Res. Appl.*, 2013, **21**, 82-87.
- 2 A. Chirila, S. Buecheler, F. Pianezzi, P. Bloesch, C. Gretener, A. R. Uhl, C. Fella, L. Kranz, J. Perrenoud, S. Seyrling, R. Verma, S. Nishiwaki, Y. E. Romanyuk, G. Bilger and A. N. Tiwari, *Nat. Mater.*, 2011, **10**, 857-861.
- 3 T. K. Todorov and D. B. Mitzi, *Eur. J. Inorg. Chem.*, 2010, **1**, 17-28.
- 4 Q. Guo, G. M. Ford, R. Agrawal and H. W. Hillhouse, *Prog. Photovoltaics: Res. Appl.*, 2013, **21**, 64-71.
- 5 P. Jackson, D. Hariskos, E. Lotter, S. Paetel, R. Wuerz, R. Menner, W. Wischmann and M. Powalla, *Prog. Photovoltaics: Res. Appl.*, 2011, **19**, 894-897.
- 6 I. Repins¹, M. A. Contreras, B. Egaas, C. DeHart, J. Scharf, C. L. Perkins, B. To and R. Noufi, *Prog. Photovoltaics: Res. Appl.*, 2008, **16**, 235-239.
- 7 J. B. Li, V. Chawla and B. M. Clemens, *Adv. Mater.*, 2012, **24**, 720-723.
- 8 A. Redinger, D. M. Berg, P. J. Dale and S. Siebentritt, *J. Am. Chem. Soc.*, 2012, **133**, 3320-3323.
- 9 J. J. Scragg, J. T. Watjen, M. Edoff, T. Ericson, T. Kubart and C. P. Bjorkman, *J. Am. Chem. Soc.*, 2013, **134**, 19330-19333.
- 10 B. Shin, O. Gunawan, Y. Zhu, N. A. Bojarczuk, S. J. Chey and S. Guha, *Prog. Photovoltaics: Res. Appl.*, 2013, **21**, 72-76.
- 11 J. J. Scragg, T. Ericson, X. Fontané, V. I. Roca, A. P. Rodríguez, T. Kubart, M. Edoff and C. P. Björkman, *Prog. Photovoltaics: Res. Appl.*, 2014, **22**, 10-17.
- 12 S. Ahmed, K. B. Reuter, O. Gunawan, L. Guo, L. T. Romankiw and H. Deligianni, *Adv. Energy Mater.*, 2012, **2**, 253-259.
- 13 Y. Cao, M. S. Denny, Jr., J. V. Caspar, W. E. Farneth, Q. Guo, A. S. Ionkin, L. K. Johnson, M. Lu, I. Malajovich, D. Radu, H. D. Rosenfeld, K. R. Choudhury and W. Wu, *J. Am. Chem. Soc.*, 2012, **134**, 15644-15647.
- 14 T. K. Todorov, J. Tang, S. Bag, O. Gunawan, T. Gokmen, Y. Zhu and D. B. Mitzi, *Adv. Energy Mater.*, 2013, **3**, 34-38.
- 15 S. Bag, O. Gunawan, T. Gokmen, Y. Zhu, T. K. Todorov and D. B. Mitzi, *Energy Environ. Sci.*, 2012, **5**, 7060.
- 16 W. Yang, H.-S. Duan, B. Bob, H. Zhou, B. Lei, C. H. Chung, S. H. Li, W. W. Hou and Y. Yang, *Adv. Mater.*, 2012, **24**, 6323-6329.
- 17 S. E. Habas, H. A. S. Platt, M. F. A. Hest and D. S. Ginley, *Chem. Rev.*, 2010, **110**, 6571-6594.
- 18 Q. Guo, G. M. Ford, W. C. Yang, B. C. Walker, E. A. Stach, H. W. Hillhouse and R. Agrawal, *J. Am. Chem. Soc.*, 2010, **132**, 17384-17386.

- 19 W. Wang , M. T. Winkler , O. Gunawan , T. Gokmen , T. K. Todorov , Y. Zhu and D. B. Mitzi, *Adv. Energy Mater.*, 2013, DOI: 10.1002/aenm.201301465.
- 20 T. K. Todorov, K. B. Reuter and D. B. Mitzi, *Adv. Mater.*, 2010, **22**, E156–E159.
- 21 W. Yang, H.-S. Duan, B. Bob, B. Lei, S.-H. Li and, Y. Yang, *Proceedings of the 38th IEEE Photovoltaic Specialists Conference*, 2012, pp. 002664-002667.
- 22 C. J. Hsu, H.-S. Duan, W. Yang, H. Zhou and Y. Yang, *Adv. Energy Mater.*, 2013, DOI: 10.1002/aenm.201301287.
- 23 Z. Su, K. Sun, Z. Han, H. Cui, F. Liu, Y. Lai, J. Li, X. Hao, Y. Liu and M. A. Green, *J. Mater. Chem. A.*, 2014, **2**, 500.
- 24 M. Jiang, F. Lan, X. Yan and G. Li, *Phys. Status Solidi RRL*, 2013, 1–5.
- 25 T. Schnabel, M. Low and E. Ahlswede, *Sol. Energy Mater. Sol. Cells*, 2013, **117**, 324–328.
- 26 K. Woo, Y. Kim, W. Yang, K. Kim, I. Kim, Y. Oh, J. Kim and J. Moon, *Sci. Rep.*, 2013, **3**, 3069.
- 27 F. Jiang, S. Ikeda, T. Harada and M. Matsumura, *Adv. Energy Mater.*, **2013**, DOI: 10.1002/aenm.201301381.
- 28 K. Woo, Y. Kim, J. Moon, *Energy Environ. Sci.*, 2012, **5**, 5340
- 29 S.-N. Park, S.-J. Sung, D.-H. Son, D.-H. Kim, M. Gansukh, H. Cheong and J.-K. Kang, *RSC Adv.*, 2014, **4**, 9118–9125
- 30 T. K. Chaudhuri and D. Tiwari, *Sol. Energy Mater. Sol. Cells*, 2012, **101**, 46–50.
- 31 Z. Su, K. Sun, Z. Han, F. Liu, Y. Lai, J. Li and Y. Liu, *J. Mater. Chem.*, 2012, **22**, 16346.
- 32 P. A. Fernandes, P. M. P. Salome and A. F. da Cunha, *J. Phys. D: Appl. Phys.*, 2010, **43**, 215403.
- 33 A. Fairbrother, X. Fontane, V. I. Roca, M. E. Rodriguez, S. L. Marino, M. Placidi, L. C. Barrio, A. P. Rodriguez and E. Saucedo, *Solar Energy Mater. Sol. Cells*, 2013, **112**, 97–105.
- 34 P.A. Fernandes, P.M.P. Salome and A.F. da Cunha, *J. Alloy. Compd.*, 2011, **509**, 7600– 7606.
- 35 X. Fontane, L. C.-Barrio, V. I.-Roca, E. Saucedo, A. P.-Rodriguez, J. R. Morante, D. M. Berg, P. J. Dale and S. Siebentritt, *Appl. Phys. Lett.*, 2011, **98**, 181905-1.
- 36 K. Nanda, *J. Phys.*, 2009, **72**, 4.
- 37 R. M. German, P. Suri and S. Park, *J. Mater. Sci.*, 2009, **44**, 1–39.
- 38 S. Chen, J.-H. Yang, X. G. Gong, A. Walsh and S. H. Wei, *Phys. Rev. B*, 2010, **81**, 245204.
- 39 D. B. Mitzi, O. Gunawan, T. K. Todorov, K. Wang and S. Guha, *Sol. Energy Mater. Sol. Cells*, 2011, **95**, 1421–143634.
- 40 J. T. Watjen, J. J. Scragg, T. Ericson, M. Edoff and C. P. Bjorkman, *Thin Solid Films*, 2013, **535**, 31–34.
- 41 O. Gunawan, T. Gokmen, B. Shin and S. Guha, *Proceedings of the 38th IEEE Photovoltaic Specialists Conference*, 2012, pp. 003001-003003.
- 42 O. Gunawan, T. Gokmen, C. W. Warren, J. D. Cohen, T. K. Todorov, D. A. R. Barkhouse, S. Bag, J. Tang, B. Shin and D. B. Mitzi, *Appl. Phys. Lett.*, 2012, **100**, 253905.
- 43 T. K. Todorov, O. Gunawan, S. J. Chey, T. G. de Monsabert, A. Prabhakar and D. B. Mitzi, *Thin Solid Films*, 2011, **519**, 7378–7381.
- 44 A.G. Aberle, S.R. Wenham and M.A. Green, *Proceedings of the 38th IEEE Photovoltaic Specialists Conference*, 1993, pp. 133–139

Table 1. Device performance of CZTS solar cells fabricated using two different precursor inks

Sample name	J_{sc} (mA cm ⁻²)	V_{oc} (V)	Fill Factor (%)	Efficiency (%)	R_s ^{a)} ($\Omega \cdot \text{cm}^2$)	R_{sh} ^{b)} ($\Omega \cdot \text{cm}^2$)
ZM hybrid ink-derived film	26.95	0.56	55.17	8.17	2.84	1339.94
ZS hybrid ink-derived film	27.15	0.49	40.28	5.38	13.15	1626.61

^{a)} Series resistance (R_s) is determined on the basis of voltage difference at the maximum power points between the one-sun J - V curve and the dark J - V curve, which is shifted by the short circuit current density J_{sc} , as proposed by Aberle.⁴⁴

^{b)} Shunt resistance (R_{sh}) is the change in the voltage for change in the current density at 0 V on the dark J_{sc} - V_{oc} curve.

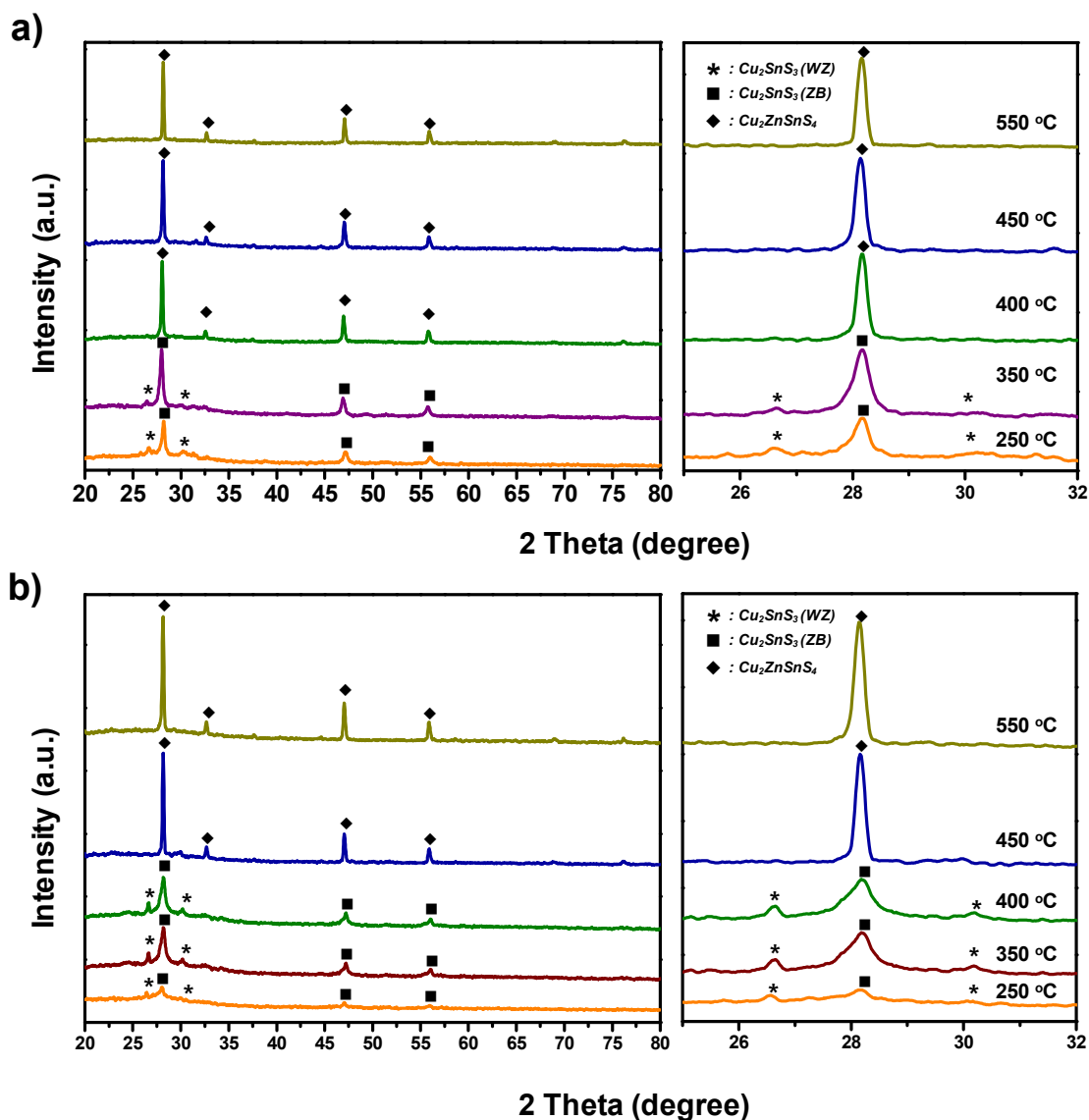


Fig. 1 XRD patterns of (a) the ZM hybrid ink-derived film and (b) the ZS hybrid ink-derived film as function of sulfuration temperatures ranging from 250 °C to 550 °C with a scan range from 20° to 80° (left side). Enlarged graphs in the 2θ range from 25° to 33° (right side) show traces of secondary phases.

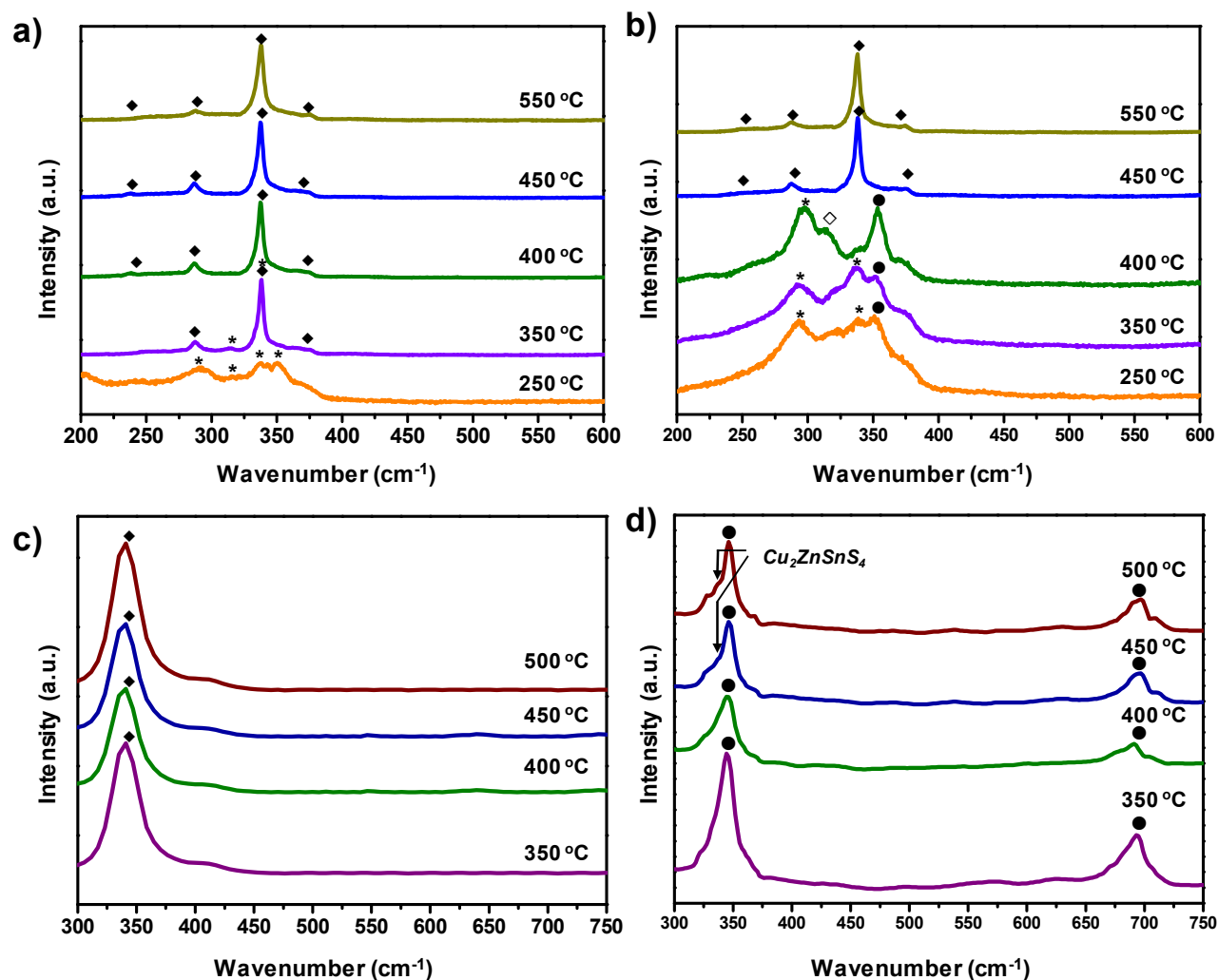


Fig. 2 Raman scattering spectra of hybrid ink-based precursor films as a function of the sulfurization temperatures ranging from 250 °C to 550 °C with a 514 nm excitation wavelength: (a) ZM hybrid ink-derived film and (b) ZS hybrid ink-derived film. Raman scattering spectra with 325 nm excitation wavelength: (c) ZM hybrid ink-derived film and (d) ZS hybrid ink-derived film (*: Cu₂SnS₃, ◆: Cu₂ZnSnS₄, ●: ZnS, and ◇: Cu₃SnS₄ (or Cu₅Sn₂S₇)).

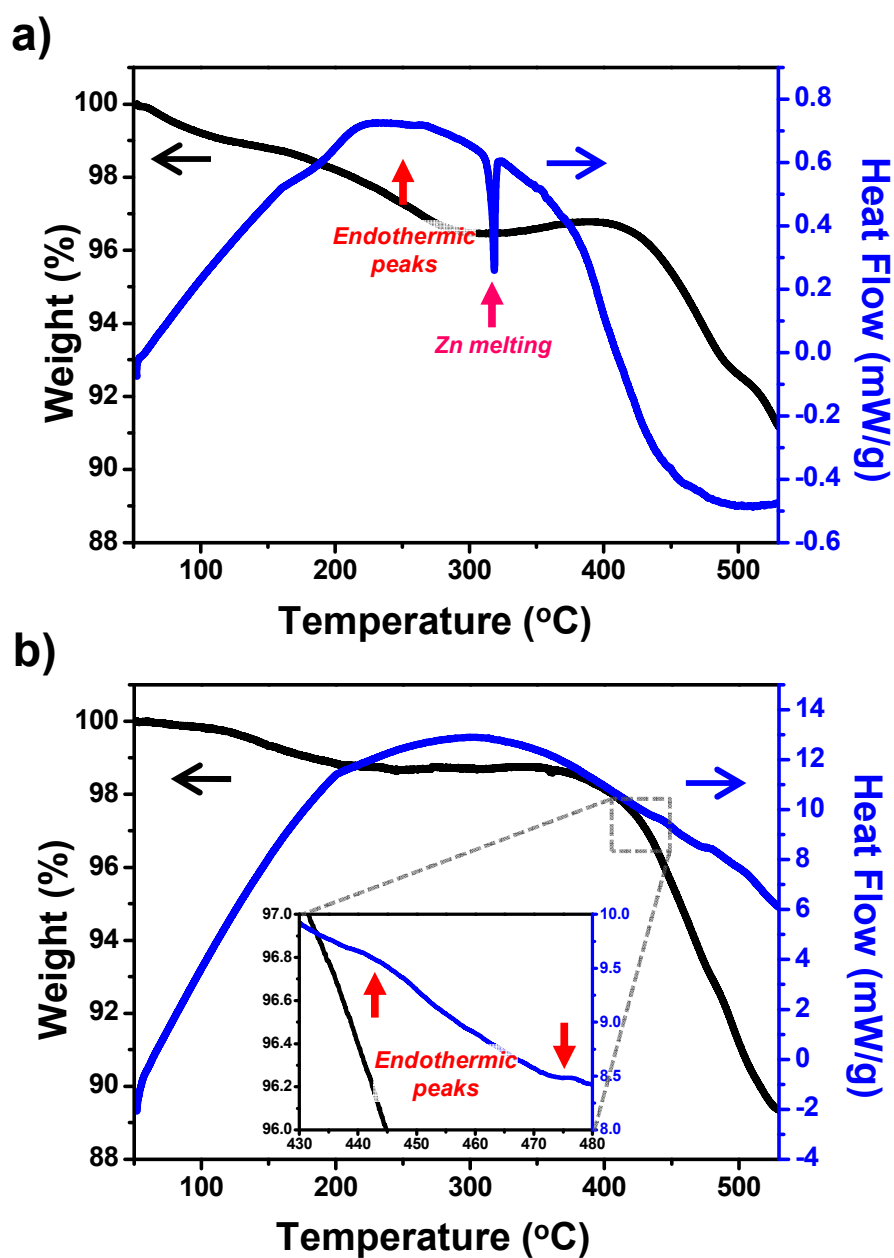


Fig. 3 TG-DSC analysis of (a) ZM hybrid precursor ink and (b) ZS hybrid precursor ink.

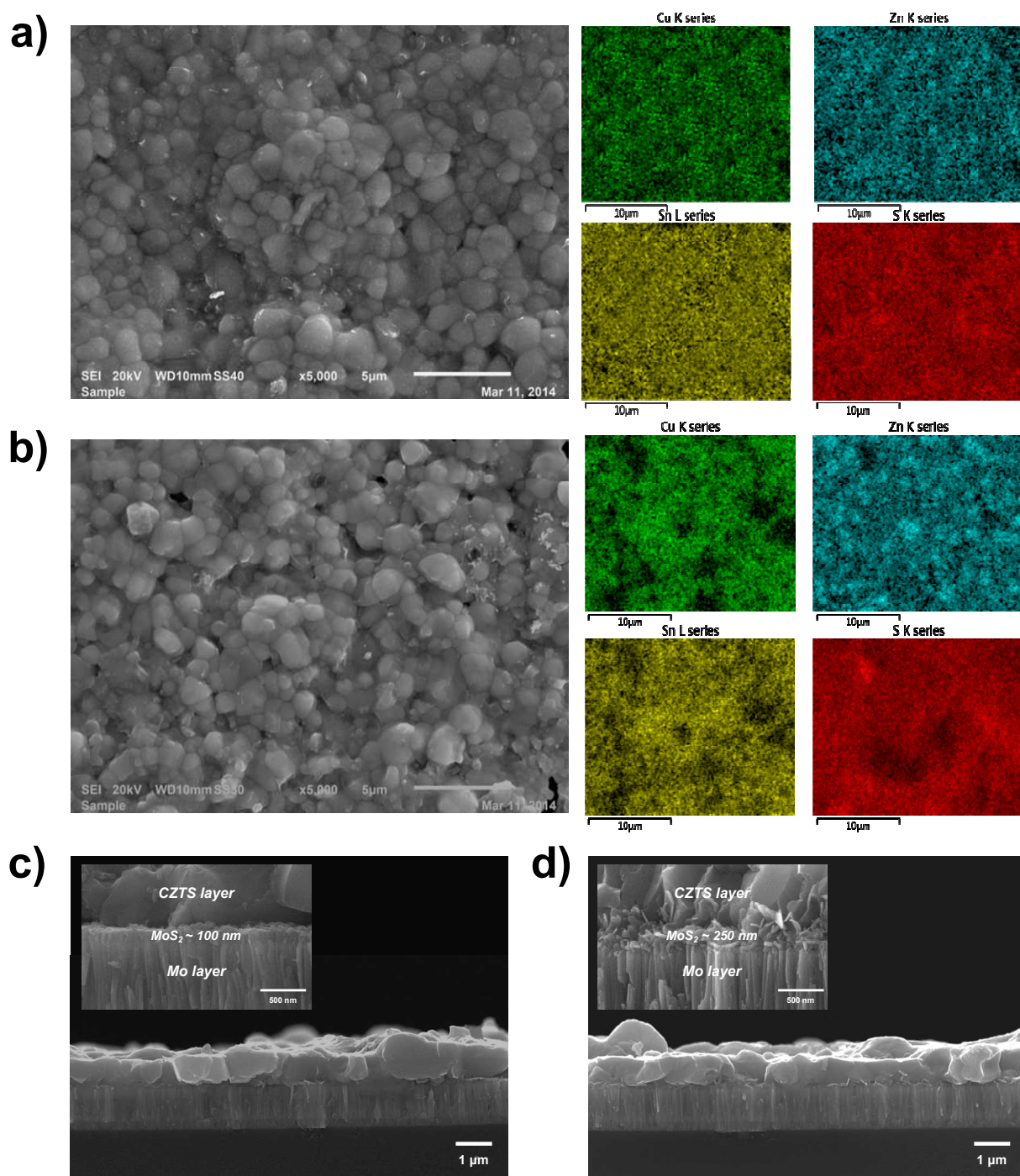


Fig. 4 Microstructure evolution and EDX composition mapping of the CZTS films annealed at 550 °C. (a) ZM hybrid ink-derived film and (b) ZS hybrid ink-derived film. Cross-sectional images of (c) ZM hybrid ink-derived film and (d) ZS hybrid ink-derived film. The interface between CZTS/Mo is shown in the inset, respectively. The precursor films were annealed under Ar + H₂S atmosphere in a tubular furnace.

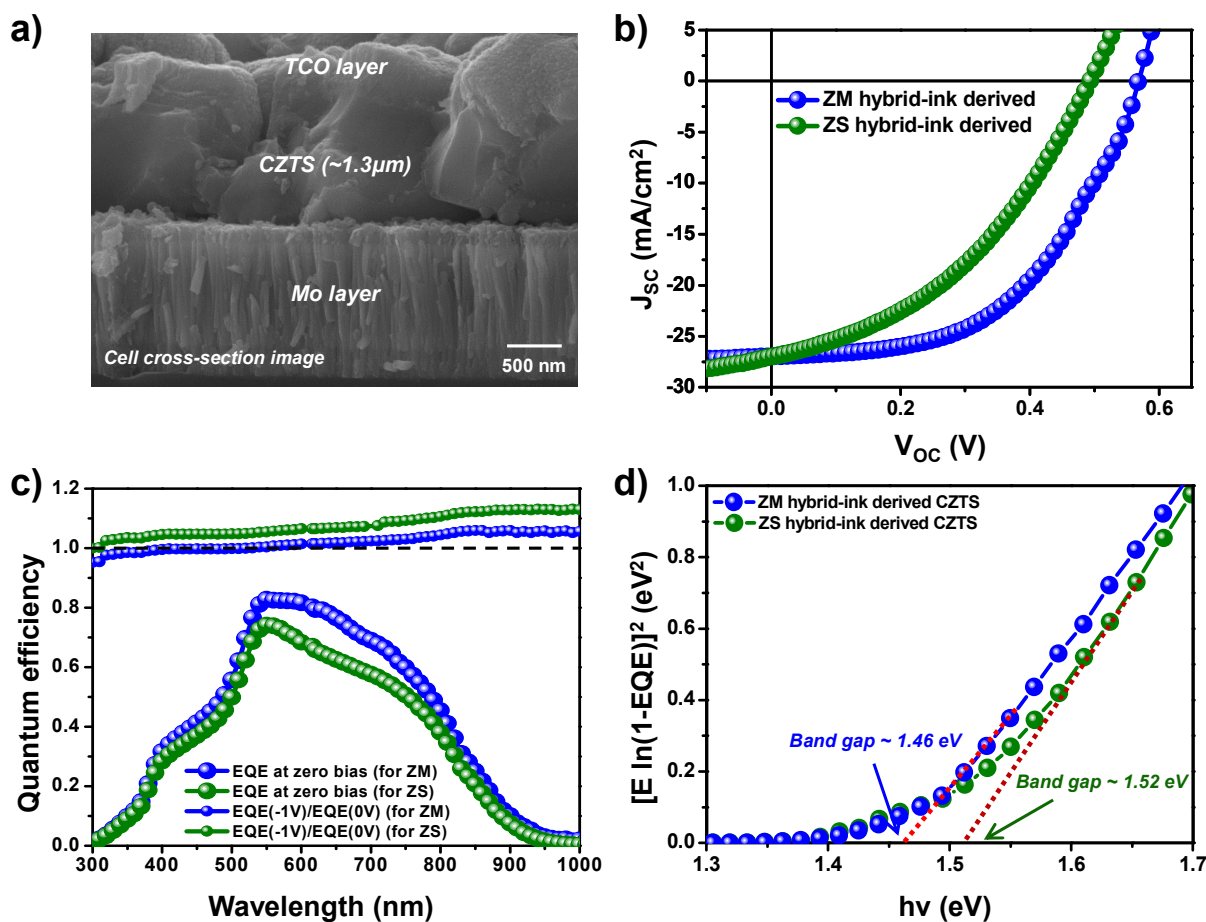


Fig. 5 (a) Cross-sectional image of the ZM hybrid ink-derived CZTS thin-film solar cell annealed at 550 °C. (b) Current density-voltage ($J-V$) characteristics of ZM hybrid ink-derived film (blue symbol) and ZS hybrid ink-derived film (green symbol) annealed at 550 °C for 30 min. The cell efficiencies are 8.17% and 5.38% under standard AM 1.5 illumination, respectively. (c) External quantum efficiency (EQE) curve of the ZM hybrid ink-derived film and ZS hybrid ink-derived film. EQE(-1.0 V)/EQE(0.0 V) of the ZM hybrid ink-derived film and of the ZS hybrid ink-derived film is also shown. (d) Band gap energy of ZM hybrid- and ZS hybrid-ink derived film annealed at 550 °C. The band gap of the absorber layer is determined using the EQE data.

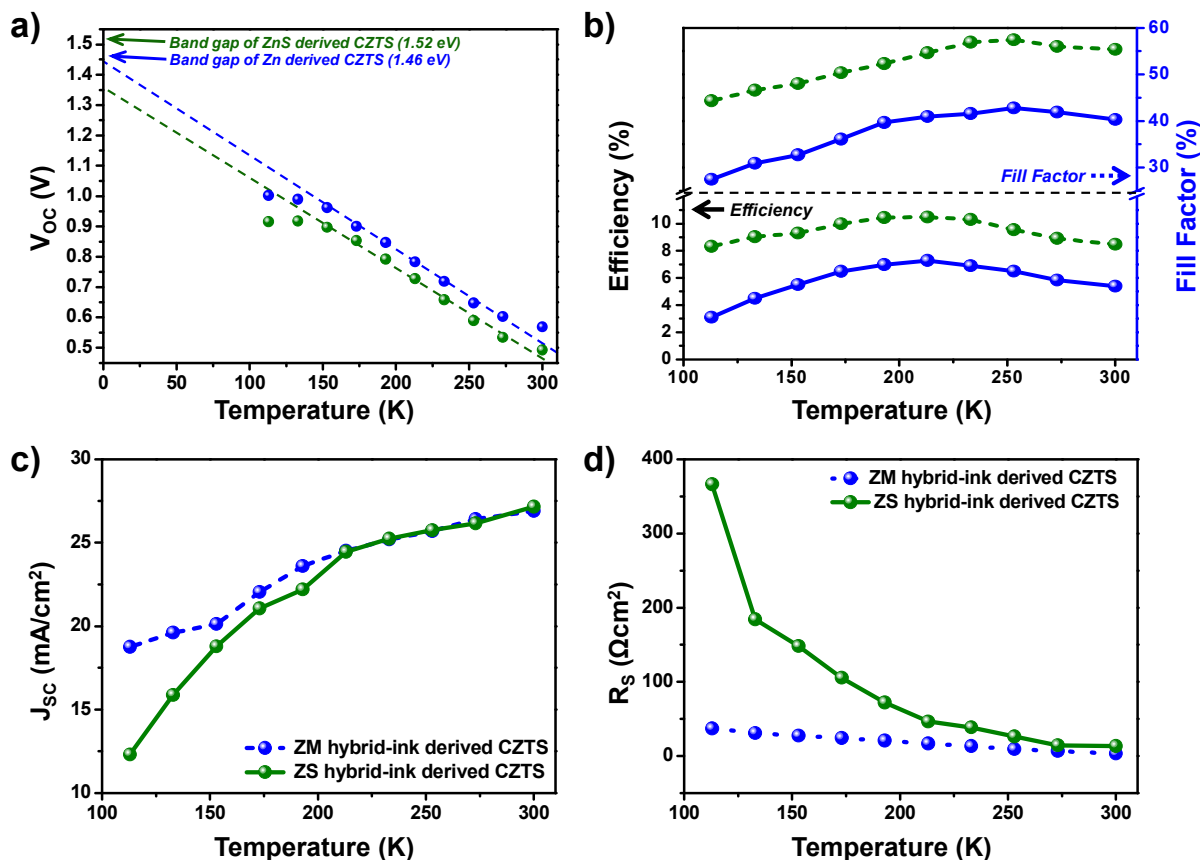


Fig. 6 Temperature-dependent characteristics for ZM hybrid-ink (blue symbol) and ZS hybrid-ink (green symbol) derived CZTS cells, respectively. Device parameters were extracted from the J - V measurement at 113 – 300 K under AM 1.5 illumination: (a) open circuit voltage (V_{oc}), showing extrapolation of the linear region to determine the activation energy for recombination, (J_{sc}), (b) efficiency and fill factor, (c) short circuit current, and (d) series resistance (R_s). R_s is estimated from the dark J - V curves using the following equation: $dV/dJ = R_s + Ak_B T/q(J - V/R_{sh})$ where, R_s , R_{sh} , A , T , q and k_B are the series resistance, shunt resistance, the diode ideality factor, temperature, electron charge, and Boltzmann constant, respectively.